Biointerface Research in Applied Chemistry
Open-Access Journal (ISSN: 2069-5837)

Article
Volume 14, Issue 6, 2024, 143
https://doi.org/10.33263/BRIAC146.143

Cabozantinib Encapsulated Lipid and Polymeric Nanoparticles: In-depth Exploration of Molecular Interactions, Formulation Strategies, and *In vitro* Studies on Hepatocellular Carcinoma

Mohammad Habeeb [1,2], Manimaran Vasanthan [1,*]

[1] Department of Pharmaceutics, SRM College of Pharmacy, SRM Institute of Science and Technology, Kattankulathur-603203, India.; manimarv@srmist.edu.in;
[2] Department of Pharmaceutics, Crescent School of Pharmacy, B.S. Abdur Rahman Crescent Institute of Science and Technology, Chennai-600048 India.; mdhabeebqa@gmail.com;
* Correspondence: manimarv@srmist.edu.in;

Scopus Author ID 36114157500
Received: 25.11.2023; Accepted: 28.01.2024; Published: 12.12.2024

Abstract: Hepatocellular carcinoma (HCC), a prime liver cancer with a high global mortality rate, has prompted the exploration of innovative therapeutic strategies, such as nanomedicine-based anticancer agents, due to the limitations of conventional chemotherapy. This study aimed to identify the most effective molecule through molecular-level interaction studies with three key anticancer pathway proteins. The selected molecule was then encapsulated with both polymer and lipid to create nanoparticles, and *in vitro* studies on HCC were conducted to assess its activity. The results of the interaction analysis revealed that Cabozantinib exhibited strong binding affinity with three proteins—folate receptor (5IZQ), vascular endothelial growth factor (5ABD), and CD44 (4PZ3)—with energies of -39.3697, -44.4525 kcal/mol, and -44.5276 kcal/mol, respectively. In the formulated nanoparticles, Cabozantinib-loaded lipid nanoparticles demonstrated higher encapsulation efficacy and drug-loading efficiency compared to their polymeric nanoformulations. *In vitro* cytotoxicity investigations indicated that Cabozantinib-loaded lipid nanoparticles displayed superior anticancer efficacy, with an IC50 value of 100.55 ± 0.05 µg/mL, as opposed to 140.65 ± 0.05 µg/mL for Cabozantinib-loaded polymeric nanoparticles against Hep3B cell lines. Additionally, fluorescence-based screening studies further affirmed the remarkable anticancer potential of Cabozantinib-loaded lipid nanoparticles, primarily through the induction of apoptosis in Hep3B cells. These findings suggest that Cabozantinib-loaded lipid nanoparticles hold promise as nanoformulations for targeting HCC.

Keywords: hepatocellular carcinoma; cabozantinib; docking; solid-lipid nanoparticle; fluorescent cell studies.

1. Introduction

Hepatocellular carcinoma (HCC), which accounts for 700,000 annual deaths from cancer, is the sixth most common cancer in the world. HCC is one of the rare malignancies whose incidence has continued to rise in recent years as a malignant tumor [1]. HCC tumors' growth and progression impede biotransformation in healthy tissues, and their mature phases result in metabolic enzyme dysregulation [2]. According to reports, HCC has a few known risk factors, such as obesity (body mass index (BMI)> 30 kg/m^2) [3]. Chronic hepatitis B virus

(HBV) and hepatitis C virus (HCV) infections, alcohol abuse, autoimmune hepatitis, diabetes mellitus, and metabolic disease [4–6]. Hepatocellular carcinoma (HCC) is a type of liver cancer that is often characterized by the expression of certain surface proteins on the cancer cells. Anticancer drugs, such as monoclonal antibodies, can target these surface proteins to help inhibit the growth and spread of cancer cells [7,8]. Liver malignancy often expresses high levels of certain surface proteins, such as CD44 antigen, which is a cell-surface glycoprotein, Epidermal Growth Factor Receptor (EGFR), fetoprotein (AFP), and glypican-3 (GPC3) and the Vascular Endothelial Growth Factor (VEGF) [9]. These proteins can be targeted with anticancer drugs, such as monoclonal antibodies or small molecule inhibitors, to slow or stop the growth and spread of HCC cells [10,11]. Combining targeted therapy with other modalities like chemotherapy and radiation therapy has demonstrated enhanced efficacy in treating HCC [12]. Cabozantinib, a multikinase inhibitor targeting VEGFR2, c-MET, AXL receptor tyrosine kinase (AXL), FLT3, c-KIT, and c-RET, gained approval in 2019 for advanced HCC patients who had prior sorafenib treatment[13]. Nanocarriers loaded with anticancer agents have shown great potential in treating various types of cancers, including HCC [14]. Nanocarriers, such as liposomes, polymeric nanoparticles, and lipid nanoparticles, are designed to encapsulate and deliver therapeutic agents to the tumor site with enriched efficacy and abridged side effects[15]. These nanocarriers offer several advantages for anticancer drug delivery. Solid lipid nanoparticles (SLNs) have substantial drug-carrying capacity and extended stability and are suitable for large-scale manufacture, making them particularly interesting as carriers for oral drug delivery applications [14,16]. Moreover, several investigations have demonstrated this [15]. They have gained considerable importance in delivering poorly soluble pharmaceuticals, such as anticancer treatments [16]. The use of different polymers to produce polymeric nanoparticles is discussed in the literature, focusing on copolymers such as PURASORB PDLG 5002A [17]. This copolymer is terminated with carboxylic acid and is composed of equal parts DL-lactide and glycolide, adhering to Good Manufacturing Practice (GMP) requirements. It is a topic of interest for research since it has an inherent viscosity midway of 0.2 dl/g in a 50/50 molar ratio [18]. The ability of PDLG-derived polymeric nanoparticles to increase the stability and solubility of medicinal medications is well known [19]. These nanoparticles have the ability to biodegrade into monomers of lactic and glycolic acids, which the body then metabolizes via the Krebs cycle before excreting carbon dioxide and water. They thus show extremely low systemic toxicity in biological systems. A large body of literature highlights the use of PDLG nanoparticles to successfully deliver several anticancer medicines and their encapsulation in both *in vitro* (lab) and in vivo tests [20]. Computational methods such as molecular docking and dynamics studies are used to forecast how pharmaceutical medicines and other small molecules will interact with certain cell surface receptors. These methods are helpful in the setting of hepatocellular carcinoma (HCC) in order to find possible new therapeutic targets for the treatment of this type of liver cancer [21,22]. By analyzing the interactions between the molecule's atoms and the receptor, docking simulations predict when a tiny molecule will bind to a receptor [23,24]. On the other hand, dynamic studies can predict the way in which the chemical and receptor interact over time [25,26]. Combined, these techniques provide important new information on the safety and possible efficacy of novel medications intended to treat HCC [27,28]. In this research, we prepared nanoparticles loaded with Cabozantinib using lipid and polymeric and compared the physical properties and *in-vitro* evaluation studies.

2. Materials and Methods

2.1. Compilation of small molecules and proteins.

The first step towards achieving the study's goals is to collect natural and artificial active substances that target HCC. The PubChem database (https://pubchem.ncbi.nlm.nih.gov/) provided nine active chemicals, as listed in (Table 1), in.sdf file format. These agents were then transformed into 3D coordinate files using BIOVIA Discovery Studio v 2021. In addition, the RCSB database (https://www.rcsb.org/) was used to retrieve the target proteins linked to HCC, specifically CD44 (PDB ID: 4PZ3), folate receptors (PDB ID: 5IZQ), and VEGF (PDB ID: 5ABD-VEGF) in.gz format. After being imported into the Discovery Studio software's graphical interface, these secondary structures—which included the crystal structures of the human CD44 hyaluronan binding domain, the human folate receptor alpha domain, and the human VEGFR-1 DOMAIN 2—were then put through an energy minimization procedure [29].

Table 1. Structure of different anticancer agents intended for HCC.

Name of anticancer agents	Chemical Structure	Name of anticancer agents	Chemical Structure
Sorafenib	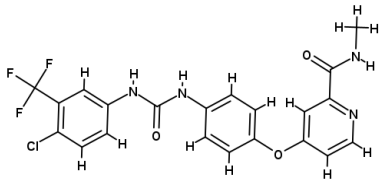	Regorafenib	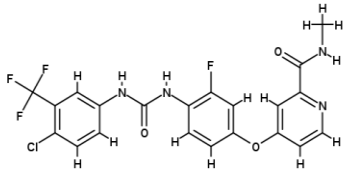
Quercetin	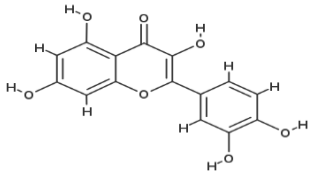	Curcumin	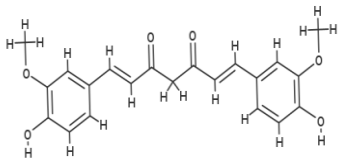
Resveratrol	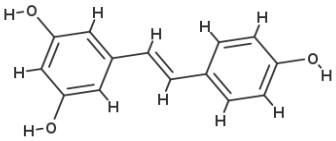	Hesperidin	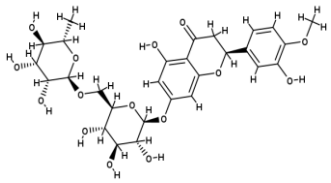
Cabozantinib	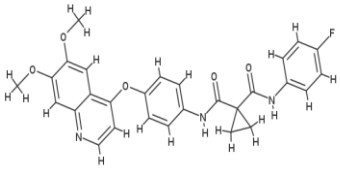	Lenvatinib	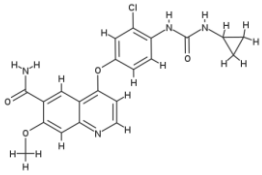

2.2. Protein and ligand modulation and energy minimization.

Molecules and proteins have an innate tendency to adopt structures that need the least amount of energy, both in nature and in our biological systems. We decided to use an inventive minimization technique in conjunction with the CHARMm force field to guarantee the stability of both molecules and proteins. This method uses the force field to evaluate the protein and molecule's starting potential energy and root mean square (RMS) values. As shown in (Table 2), the smart minimization technique uses two algorithms—steepest descent and conjugated gradient—to optimize the parameters and lower energy at the atomic level.

Table 2. Represents the parameter setup for the energy minimization.

Name of the Parameter	Setup value
Input Ligands	Molecules
Max Steps	2000
Input force field	CHARMm
Minimization Algorithm	Smart Minimizer
Dielectric Constant	1
RMS Gradient	0.01
Partial Charge Estimation	Momany-Rone
Nonbond List Radius	18.0

2.3. Modules for software and c-docker.

Discovery Studio v17 simulation software was utilized to investigate the interaction patterns at the atomic level between macromolecules and proteins. The work applied the Minimization and C-Docker modules to extensively examine the interactions and energy inside the complexes. The CHARMm force field was initially pragmatic to eight ligands (gathered from PubChem) and three proteins (folate receptor 5IZQ, 5ABD-VEGF, and CD44 - 4PZ3) during the docking pre-preparation. This attempted to quantify potential energy and repair inaccuracies at the atomic. During the first step, the energy of the molecules was minimized to local minima using the smart minimizer algorithm and a spherical cut-off method. As shown in **(**Table 3), this process involved 1000 maximum steps, a 0.1 RMS gradient, and a 14.0 non-bonded radius. Furthermore, the protein's energetic site was chosen based on the PDB site record. The c-docker module algorithm was used under specified conditions to predict the best binding molecule with distinct proteins [30].

Table 3. Represents parameters and settings for the C-Docker protocol settings for docking.

Protocol	Setting
Input ligands	biomolecules
Input receptor	5IZQ, 5ABD, 4PZ3
Pose cluster radius	0.1
Top selection	10
Random conformations	10
Molecular dynamics steps	1000
Target temperature	1000
Incorporate electrostatic interactions	TRUE
Orientations for refinement	10
vdW energy threshold for orientation	300
Maximum unfavorable orientations	800

2.4. Molecular mechanisms research.

The stability of Cabozantinib docked complexes, including (CD44-4PZ3), (folate receptors-5IZQ), and (5ABD-VEGF), was evaluated using the Desmond module of Schrodinger 2021-4. A molecular dynamics investigation was carried out for 100 nanoseconds, recording trajectories at 100 picosecond intervals and producing and analyzing 1000 conformations. The NPT ensemble was used in the simulation at a temperature of 300K and a pressure of 1.03215 bar. The RESPA integrator maintained a time step of 2.0 femtoseconds with a Coulombic interaction cut-off radius 9. The explicit solvent system and OPLS3 force field were used to investigate the complex within Schrodinger 2021-4's Desmond module [31].

3. Materials

Purasorb PDLG 5002A, a copolymer composed of carboxylic acid-terminated 50:50 DL-lactide: glycolide with a midway intrinsic viscosity of 0.2 dl/g, was generously donated by Corbion Purac for the manufacture of nanoparticles. PVA (with a molecular weight range of 30,000-70,000 and 87-90% hydrolysis), Polysorbate 80, acetone, and phosphate-buffered saline (PBS) were among the materials obtained from Sigma Aldrich in St. Louis, MO, USA. Compritol® 888 and Gelucire® 50/13 emulsifiers and co-emulsifier Labrafil® M2125CS were obtained as free samples from Gattefosse in Saint-Priest, France. Alembic Pharma Limited Hyderabad provided Cabozantinib. Hep3B hepatocellular carcinoma cell lines were obtained from the American Type Culture Collection (ATCC) in Manassas, VA, and were cultured in minimum essential medium (MEM). The growth media for all cultures included 10% fetal bovine serum (FBS), along with penicillin (100 units/mL) and streptomycin (100 g/mL). The cells were maintained in a humidified environment at 37°C with 5% CO_2.

3.1. Fabrication of Cabozantinib-loaded polymeric nanoparticles (CPNs).

Using magnetic stirring, 5 to 10 mg of Purasorb® PDLG 5002A and 0.5 to 4 mg of Cabozantinib were dissolved in 0.5 to 1.0 mL of acetone. An aqueous solution (0.5 to 2.0% w/v) comprising emulsifying agents such as polysorbate 80 and poly(methacrylic acid sodium salt) was used to prepare a water phase ranging in volume from 2.0 to 4.0 mL. This water phase was injected into the organic phase all at once. The organic solvent was then allowed to evaporate for 12 hours at room temperature and 1 bar pressure with constant stirring. The nanoparticles were centrifuged for 25 minutes (Eppendorf 5424 R, Hamburg, Germany), washed three times, and redispersed in an equal volume of purified water [32].

3.2. Manufacturing of Cabozantinib-loaded solid lipid nanoparticles (CSLNs).

CSLNs were created using a high-energy technique that produced distinct aqueous and oil phases. The oil phase was heated and held at 80°C until complete melting of Compritol (1500 mg), labrafil (150 mg), Gelucire (1350 mg), and Cabozanitib (60 mg). Using an Ultra-Turrax T25 (IKAWerke, Saufen, Germany), the aqueous phase (20 mL of PBS) was gradually added to the oil phase at the same temperature (80°C) while rapidly stirring at 10,000 rpm for 10 minutes. The resultant product was then disseminated in PBS and either homogenized or sonicated with a solvent [33].

3.3. Assessment of the hydrodynamic size (HD), polydispersity index (PDI), and zeta potential.

Over a 120-day period, the hydrodynamic diameter, polydispersity index (PDI), and zeta potential of CPNs and CSLNs were determined using Dynamic Light Scattering (DLS) with a Zeta Sizer (Nano ZS, Malvern Instruments, UK). The results were obtained after diluting the samples 1:20 with distilled water [34].

3.4. Drug entrapment efficiency and drug loading measurements.

The percentage of entrapment efficiency (% EE) and the percentage of drug loading (% DL) were determined to determine drug entrapment efficiency. The nano-formulations were tested by centrifuging the samples for 30 minutes at 30°C and 15000 rpm. After centrifugation,

the free quantity of SFB in the supernatant was measured using a UV-Vis spectrophotometer at 244 nm. The following formulas were used to calculate % EE and % DL for the nano-formulations of CPLNs and CSLNs[35].

3.5. FTIR (Fourier transform infrared spectroscopy).

The alterations in the functional groups of the samples were studied using Fourier Transform Infrared Spectroscopy (JASCO 6300) at Crescent Institute of Science and Technology's core instrumentation facility in Chennai, India. The ATR (attenuated total reflections) method was used to obtain FTIR spectra for PDLG 5002A, Compritol 888, RT, CPLNs, and CSLNs. The FTIR spectra were obtained across a range of 4000-400 cm^{-1} with a resolution of 4 cm^{-1} and an average of 50 scans [36].

3.6. In-vitro drug release.

In order to assess the drug release from encapsulated NP solutions of CPNs and CSLNs, which had a 10 mL volume and an equivalent concentration of 0.1 mg/mL, dialysis was carried out in 50 mL of phosphate-buffered saline (pH 7.4, 0.2% Tween 80). Molecular-weight cut-off tubes (Spectrum, 14 kD) were used for dialysis. The tubes were shaken constantly in an orbital water bath at 37°C. The release media was removed at certain intervals and replaced with the new medium. The medication released from CPLNs and CSLNs was quantified at a wavelength of 244 nm using a UV-Vis spectrometer (Shimadzu, UV-2700). Furthermore, by dialyzing against PBS (pH 7.4) in the presence of 20% (v/v) FBS, drug release patterns were predicted [37].

3.7. MTT investigation.

CPNS and CSLNs were tested for *in vitro* cytotoxicity using the MTT (3-(4,5-dimethylthiazol-2-yl)-2,5-diphenyltetrazolium bromide) assay. First, cells were seeded at a density of 4000–5000 cells per well in 96-well plates with flat bottoms. The plates were then incubated at 37°C for 24 hours. The cells were then exposed to different concentrations of CPT-11, free Cabozantinib, CSLNs, and CPNs-formulated nanoparticles. This was followed by an extra 72 hours of incubation at 37°C. Following this incubation, each well received 30 µL of MTT solution (5 mg/mL in PBS). After four hours, 100 µL of DMSO was added to the purple MTT-formazan crystals to solubilize them. The absorbance in every well was determined at 490 nm using a Multiskan FC microplate reader from Thermo Scientific [37].

3.8. Fluorescent cell investigations.

3.8.1. Annexin V-Cy3 assay.

During the early stages of apoptosis, phosphatidylserine is relocated from the inner to the outer layer of the plasma membrane. To identify the presence of cell surface phosphatidylserine, annexin V labeled with Cy3 was employed, using the annexin V-Cy3 apoptosis detection kit (APOAC) commercially available from Sigma-Aldrich, St. Louis, MO, USA. Cells treated with the 24-hour IC50 of pure Cabozantinib, CSLNs, and CPNs underwent washing with cold phosphate-buffered saline. Subsequently, they were exposed to a 50 µL double label-staining solution containing 1 µg/mL annexin-Cy3 and 100 µM 6-carboxyfluorescein diacetate (6-CFDA) for 10 minutes at room temperature in the dark.

Following a wash with 1× binding buffer, 300 randomly selected cells were observed using a fluorescent microscope. The co-application of 6-CFDA with annexin V-Cy3 facilitated the identification of live cells (green), necrotic cells (red), and apoptotic cells (red nuclei and green cytoplasm) [38].

4. Results and Discussion

4.1. Protein-Ligand Interaction investigations.

Molecular interaction experiments were performed on 5IZQ, 5ABD, and 4PZ3 proteins utilizing a force field and minimization technique. The energy levels found to be steady were -111,388 kcal/mol, -18,300.20 kcal/mol, and -19,367 kcal/mol, in that order. For each of the three proteins, the binding pocket algorithm produced a red, spherical binding pocket (Figures 1A, 1B, and 1C). The optimal binding positions of a molecule in these proteins' cavities were obtained using the CHARMm-based docking procedure. As shown in Table 4. The results of the docking analysis involving eight bioactive molecules indicated that Cabozantinib adopted the appropriate conformation through interaction with the active site amino acid. The affinity levels for Cabozantinib were observed to be -39.3697 kcal/mol, -44.4525 kcal/mol, and -44.5276 kcal/mol across the three specified proteins, as summarized in Table 4.

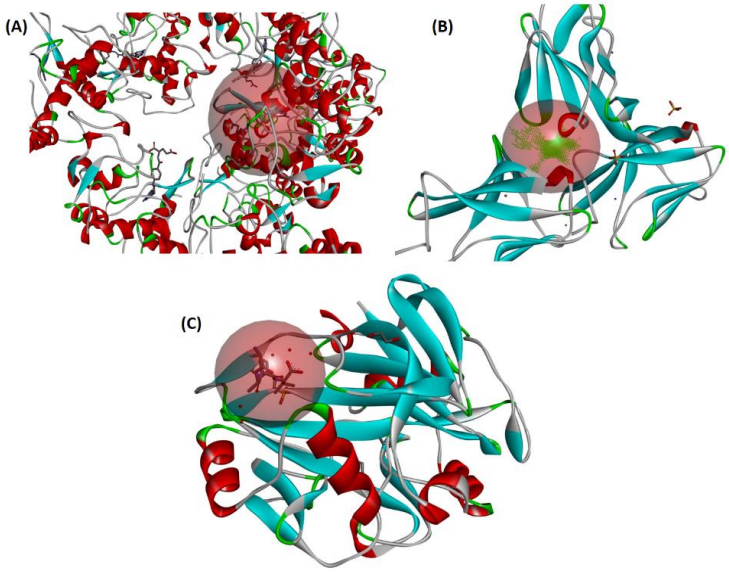

Figure 1. (A) Shows the secondary structure of protein 5IZQ with its corresponding binding pocket; **(B)** the Secondary structure of protein 4PZ3 along with its binding pocket; **(C)** Exhibits the secondary structure of protein 5ABD, including its binding pocket.

Table 4. Various energies and docking energy of the drug molecules with proteins

Name	Initial RMS gradient	Initial Potential Energy	Final Potential Energy	Electrostatic Energy	Final RMS gradient	vdW energy	Dock energy
5IZQ	2,030.03	-30,001	-111,388	-114,974	1.08551	-12,386	--
Cabozantinib	633.467	825.447	-25.7573	-26.8567	0.00989	9.40363	-39.3697
Curcumin	35.5349	57.0782	-14.9832	-39.9431	0.00811	1.53772	-23.9331
Hesperidin	41.5762	255.271	43.7045	-29.2294	0.00824	-5.2129	-18.7501
Lenvatinib	86.1218	2,260.19	-11.7979	-49.0770	0.00951	9.4321	-17.9617
Quercetin	41.8441	70.8223	-7.83907	-18.7376	0.00899	2.71704	-22.5115
Regorafenib	100.030	160.611	-14.9488	-43.8235	0.00981	7.29573	-29.7701
Resveratrol	39.5805	44.9756	3.1111	-9.1212	0.00799	5.12522	-28.7654
Sorafenib	80.1101	144.925	-3.90478	-31.9128	0.00899	5.92525	-32.1110
5ABD	2,839.84	39,044.70	-18,300.20	-18,431	1.20381	-3,031	--
Cabozantinib	632.477	732.558	12.2524	-25.7567	0.00855	9.50123	-44.4525

Name	Initial RMS gradient	Initial Potential Energy	Final Potential Energy	Electrostatic Energy	Final RMS gradient	vdW energy	Dock energy
Curcumin	35.1252	60.0252	-23.1732	-35.8252	0.00822	1.71211	-5.90711
Hesperidin	39.4662	270.344	43.7012	-31.8994	0.00824	-5.7130	-34.5544
Lenvatinib	84.2568	1,360.08	-11.6828	-49.0729	0.00856	9.2589	-31.3556
Quercetin	43.8241	70.6821	-5.84952	-16.78526	0.00889	1.62563	-1.70632
Regorafenib	103.025	130.498	-12.9488	-41.8525	0.00852	7.30573	-19.2125
Resveratrol	41.4252	44.6125	3.4252	-7.9863	0.00768	4.50982	-8.62347
Sorafenib	80.1524	154.127	-5.40478	-31.3128	0.00813	7.13224	-21.4514
4PZ3	35.1282	-8,454.02	-19,367	-22,161.52	0.86554	-4038.68	--
Cabozantinib	592.547	685.447	13.1574	-26.2567	0.00869	9.10363	-44.5276
Curcumin	36.5348	58.1652	-23.5742	-38.7521	0.00942	1.74882	-3.41644
Hesperidin	41.5562	275.236	43.7945	-31.2394	0.00914	-4.8129	-1.52113
Lenvatinib	88.2338	1,360.18	-9.8818	-50.0869	0.00951	9.1121	-4.85118
Quercetin	43.8541	73.8823	-5.85907	-16.6566	0.00977	1.81704	-5.97304
Regorafenib	100.030	155.708	-12.9998	-41.8235	0.00921	7.21573	-8.89703
Resveratrol	41.4515	44.5886	2.5199	-7.2263	0.00878	5.40281	-15.9463
Sorafenib	80.1524	144.167	-5.10478	-31.9121	0.00894	5.95224	-12.7774

Figure 2A illustrates the optimal binding of Cabozantinib with protein 5IZQ, where it establishes over 13 interactions with the active site amino acids. Specifically, conventional hydrogen bonds are formed between the amino acids GLNA: 100, TRP: A102, and the oxygen atom of Cabozantinib. Additionally, a carbon-hydrogen bond is formed between the amino acid SERA: 174 and the aromatic-substituted fluorine atom of Cabozantinib. Furthermore, π-π stacked and π-π alkyl bonds are observed with amino acids (TRPA: 140, TRPA: 64, TRPA: 171, TYRA: 85, TYRA: 60, PHEA: 62, LYSA: 198) of protein 5IZQ.

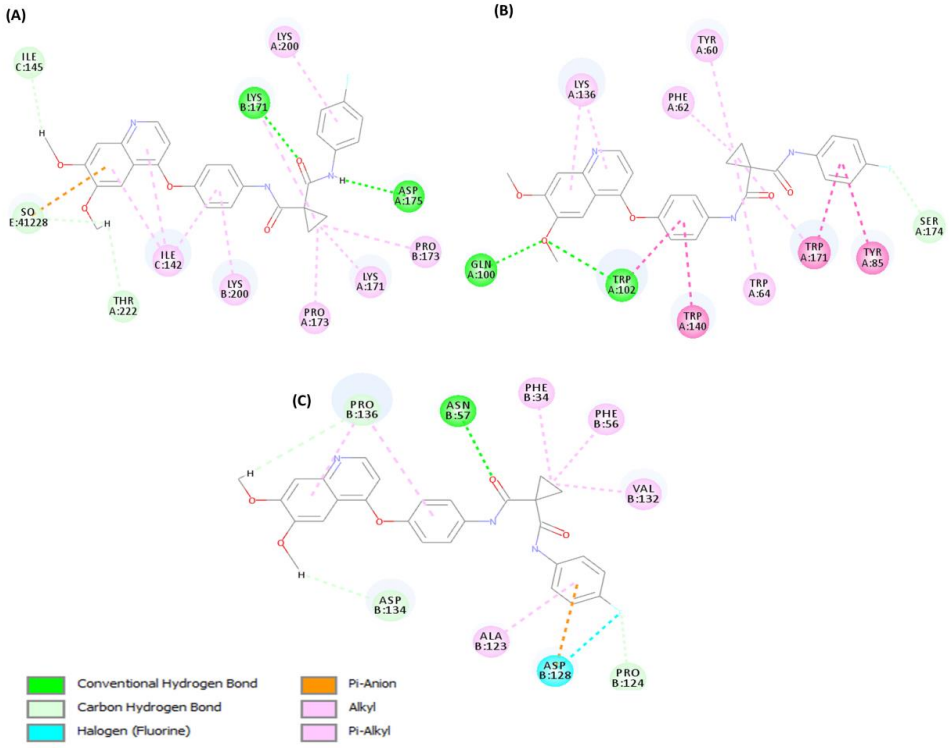

Figure 2. (A) Illustrates the interplay between the active site amino acids of protein 5IZQ and Cabozantinib; **(B)** Showcases the interaction of the active site amino acids of protein 5ABD with Cabozantinib, the most effective interacting molecule; **(C)** demonstrates the interaction of active site amino acids of 4PZ3 with Cabozantinib, the best-interacting molecule.

These interactions, along with additional energies such as bond angles, van der Waals (vdW), and electrostatic interactions, contribute to forming a stable complex with an energy of 16.9617 kcal/mol, as presented in (Table 4). In Figure 2B, the Cabozantinib molecule engages in five categorized interactions and forms 15 different bonds with the binding sites of the 5ABD receptor amino acids. Conventional hydrogen bonds are established between the amino acids LYSB: 171 and ASPA: 175, connecting with the oxygen and amine atoms of Cabozantinib, respectively. In contrast, the amino acids ILEC: 145 and THRA: 222 generate a carbon-hydrogen bond, contributing to two interactions at hydrogen atoms of the Cabozantinib molecule. Additionally, alkyl and π-alkyl interactions account for a total of nine interactions with the amino acids (ILEC: 142, LYSB: 200, PROA: 173, LYSA: 171, PROB: 173, and LYSA: 200) in the aromatic and cyclopropane ring of the Cabozantinib molecule. The synthetic drug Cabozantinib establishes 11 different categorized interactions within the binding pocket of the 4PZ3 receptor. The active site amino acid ASNB: 57 forms a conventional hydrogen bond with the oxygen atom of the Cabozantinib molecule. Additionally, amino acids PROB: 136, ASPB: 134, and PROB: 124 generate three carbon-hydrogen bonds with the atoms of the Cabozantinib molecule, as illustrated in (Figure 2C). Similarly, alkyl and π-alkyl interactions are associated with five amino acids: PROB: 136, PHEB: 34, PHEB: 56, VALB: 132, and ALAB: 123.

4.2. Molecular dynamics studies.

4.2.1. Protein-ligand RMSD for 5IZQ, 5ABD, and 4PZ3.

The root mean square deviation (RMSD) analysis of the simulation run between the 5IZQ protein and Cabozantinib indicates that the molecule stabilizes after 24 ns and achieves complete stabilization after 74 ns, as illustrated in (Figure 3A).

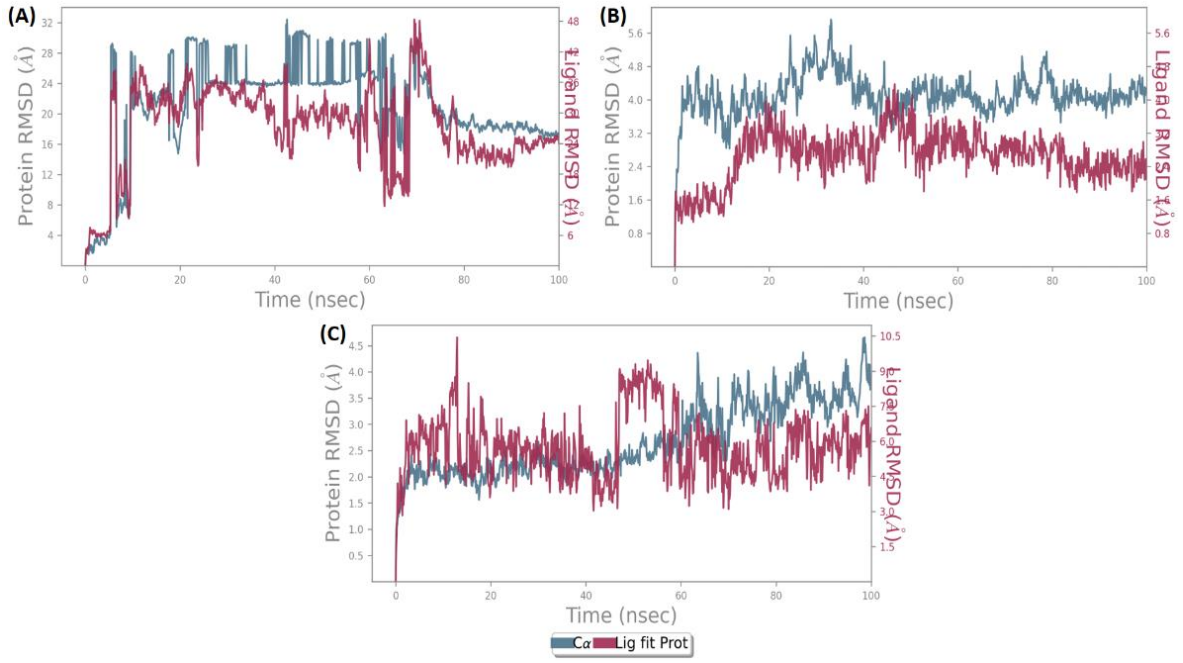

Figure 3. Illustrates the results of molecular dynamics simulations concerning Protein-ligand interactions. **(A)** Displays the root mean square deviation (RMSD) of the natural molecule Cabozantinib when interacting with the 5IZQ protein receptor; **(B)** the RMSD of the interaction between Cabozantinib and the 5ABD protein receptor is depicted. Additionally**, (C)** showcases the RMSD values reflecting the interaction of the Cabozantinib molecule with the 4PZ3 protein receptor.

Correspondingly, in the simulation run between the 5ABD protein and Cabozantinib, the Cabozantinib molecule stabilizes between 20-40 ns, followed by small fluctuations during the 40-50 ns period. Subsequently, it stabilizes up to 100 ns with an RMSD of 2.4-3.2 Å, as elucidated in (Figure 3B). In the same way, root mean square deviation analysis of the simulation run between the 4PZ3 protein and Cabozantinib shows that the Cabozantinib molecule stabilizes after 16 ns, experiences fluctuations at 47-56 ns, and achieves complete stabilization after 64 ns, as depicted in (Figure 3C).

4.2.2. Protein-ligand RMSF for 5IZQ, 5ABD, and 4PZ3.

Root mean square fluctuations (RMSF) of amino acids are presented in Figure 4A. Upon Cabozantinib binding to protein 5IZQ, noteworthy changes in high-energy fluctuations occur at the 136-138 and 144-148 amino acid residues, distinct from fluctuations in other amino acids (Figure 4A). Similarly, the interaction between Cabozantinib and protein 5ABD reveals significant alterations in high-energy fluctuations at the 42-46, 68, 72, 88-93, 138-140, 143, 163, 158-164, 182-184, and 190-201 amino acid residues, relative to other amino acids' fluctuations (Figure 4B). Additionally, Cabozantinib binding to protein 4PZ3 induces noteworthy changes in high-energy fluctuations at the 155, 158, 160, 180-182, 249, 251, 253, 257, 259-265, and 269 amino acid residues, compared to fluctuations in other amino acids (Figure 4C).

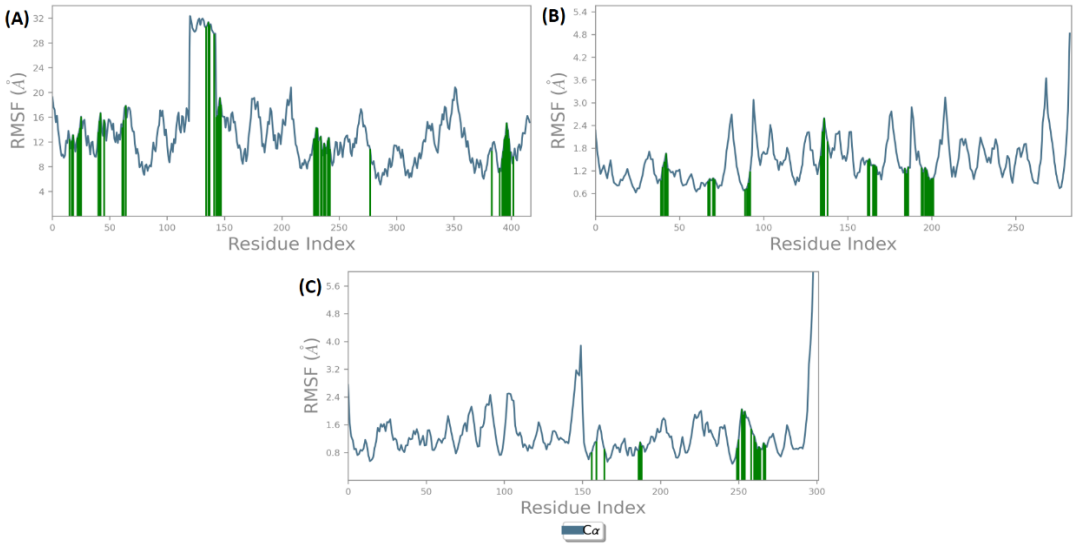

Figure 4. Represents the outcomes of molecular dynamics simulations focusing on the Protein-ligand interface. Panel **(A)** illustrates the Root mean square fluctuation (RMSF) of the natural molecule Cabozantinib in conjunction with the 5IZQ protein receptor; **(B)** the RMSF of the 5ABD protein receptor interacting with the drug molecule is depicted. Furthermore, **(C)** displays the RMSF values representing the interaction between the Cabozantinib molecule and the 4PZ3 protein receptor.

4.2.3. Ligand protein contacts for 5IZQ, 5ABD, and 4PZ3.

The simulation interaction diagram protocol run revealed how the 5IZQ complex and Cabozantinib developed stable hydrogen bonds and hydrophobic and ionic interactions with the assistance of water bridges. The interactions between the active sites of the amino acids in 5IZQ and the hydrophobic groups of Cabozantinib are predominantly mediated via hydrophobic bridges, as illustrated in (Figures 5A and 5B). Specifically, the b-chain amino acid ASP171 forms medium hydrophobic bridges and small ionic interactions with two hydrogen bonds. Due to its greater hydrophobic ring systems, the Cabozantinib molecule generated only

a few water bridges while binding. Cabozantinib formed interactions with 19 amino acids of the 5IZQ protein molecule, as detailed in **(**Supplementary File S1). The simulation interaction diagram protocol run exposed that the Cabozantinib and 5ABD complex formed stable non-bonded interactions such as hydrogen bonds, ionic interactions, and more hydrophobic interactions, along with a few water bridges due to the higher hydrophobic ring systems, as depicted in (Figures 5C and 12D). Cabozantinib formed interactions with 33 amino acids of the 5ABD protein molecule, as outlined in (Supplementary File S2).

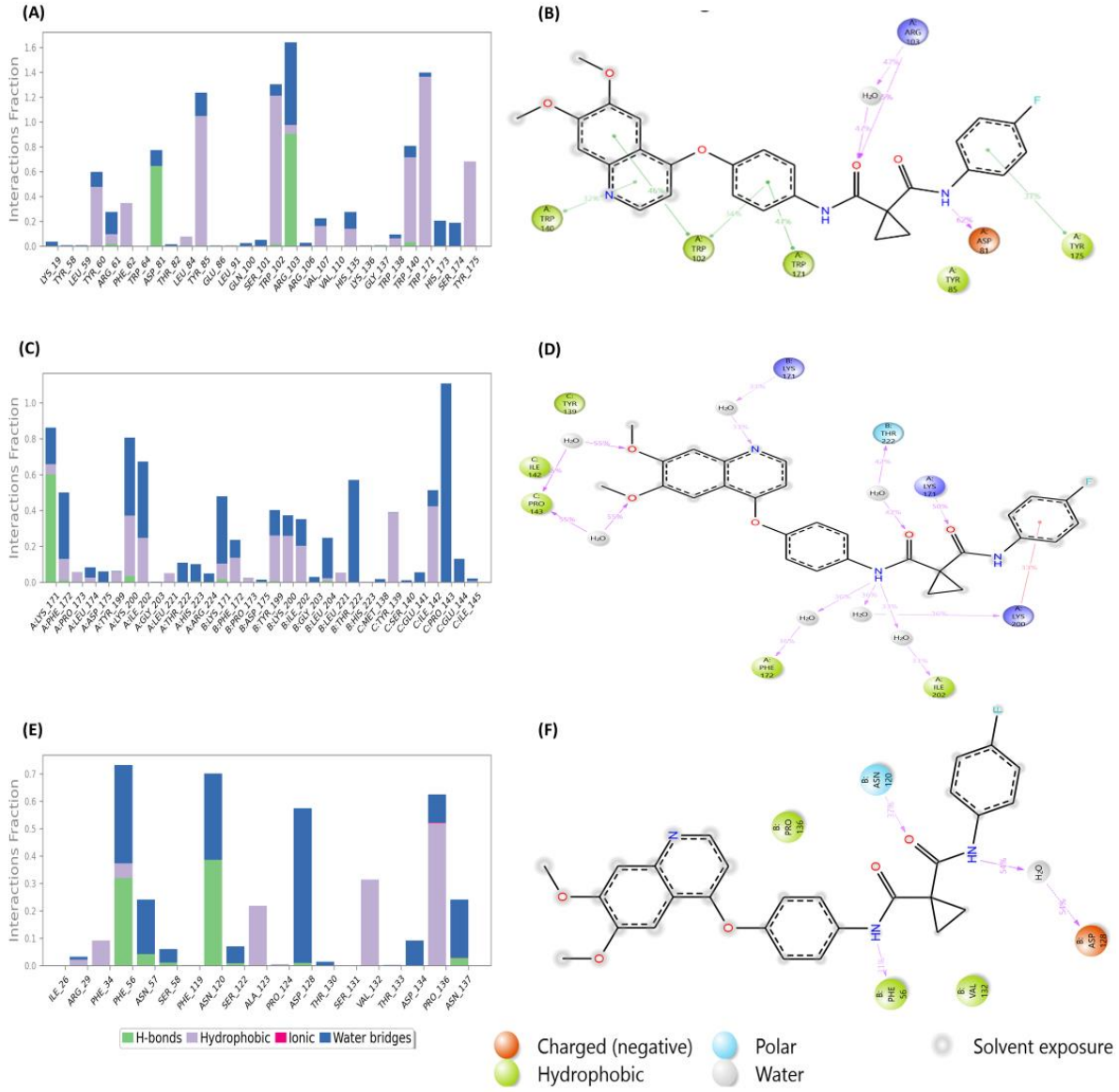

Figure 5. Presents the results of molecular dynamics simulations in the form of histograms depicting protein-ligand interactions, specifically focusing on hydrogen bonding, hydrophobic interactions, ionic interactions, and water bridges. **(A)** Histogram representation of the interactions between the protein 5IZQ and the Cabozantinib molecule; **(B)** A detailed structural representation illustrates the specific interactions between Cabozantinib ligand atoms and the protein residues of 5IZQ. Similarly, (C) and **(D)** Represent the histogram and structural representations for the interaction between the protein 5ABD and Cabozantinib. Finally, Panels **(E)** and **(F)** depict the histogram and structural details of the interactions between the protein 4PZ3 and the Cabozantinib molecule.

Similarly, the simulation interaction diagram protocol run exposed that the Cabozantinib and 4PZ3 complex formed stable non-bonded interactions, including hydrogen bonds and hydrophobic and ionic interactions, aided by water bridges. The hydrogen groups of

Cabozantinib are primarily involved in water bridge interactions with the active sites of amino acids in 4PZ3, as represented in (Figures 15E and 15F). Cabozantinib formed interactions with 29 amino acids of the 4PZ3 protein molecule, contributing to the increased stability of the Cabozantinib-protein complex (Supplementary File S3).

4.3. FTIR.

4.3.1. CPNs.

An interpretation of FTIR data comparing pure Cabozantinib, CPNs (Cabozantinib polymer formulation), and pure PDLG polymer is provided below. The wavenumber 3846.33 cm^{-1} for pure Cabozantinib suggests the presence of O-H stretching vibrations, possibly originating from phenols or alcohols illustrated in (Figure 6). In the CPNs formulation, the wavenumber 3447.13 cm^{-1} decreases in intensity compared to pure Cabozantinib, indicating potential interactions between Cabozantinib and the PDLG polymer that affect O-H stretching. The wavenumber 2923.56 cm^{-1}, typically associated with C-H stretching vibrations, suggests the presence of aliphatic hydrocarbons. The wavenumber 2045.14 cm^{-1} is considered unusual for standard organic functional groups. It could be associated with a specific functional group in Cabozantinib or PDLG or indicate an instrumental artifact. The wavenumbers 1751.06 cm^{-1} and 1673.91 cm^{-1}, often linked to C=O stretching vibrations, suggest the presence of carbonyl groups, such as those in ketones or esters and possibly due to interactions with PDLG, indicative of carbonyl groups in a different chemical context. At 1429.96 cm^{-1} in CPNs, a change in intensity may indicate interactions between C=O groups in Cabozantinib and the PDLG polymer, suggesting the presence of methyl or methylene groups. The wavenumber 1085.73 cm^{-1} in CPNs shows a decrease in intensity, suggesting interactions between C-N groups, indicative of the presence of amines or amides. 746.317 cm^{-1} of this lower wavenumber is associated with the rocking vibration of CH2 groups in the PDLG polymer. It's important to note that the exact functional group assignments can vary depending on the specific chemical structure of Cabozantinib and PDLG of nanoparticles.

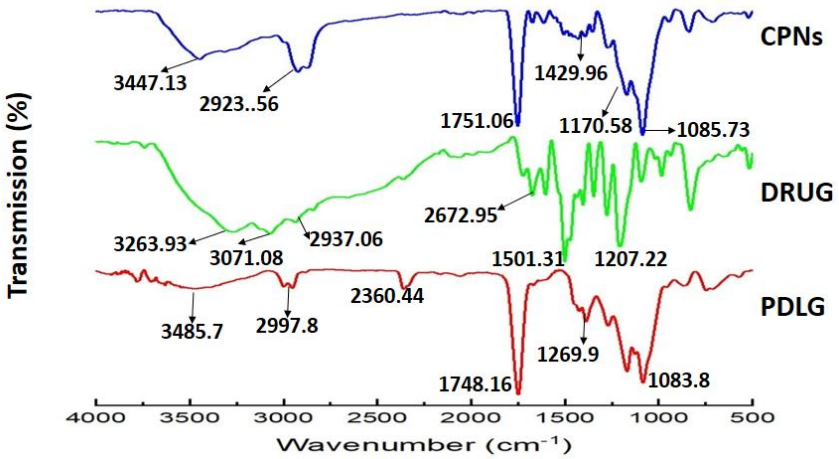

Figure 6. Illustrates FTIR spectra for the following materials: Cabozantinib in its unaltered state, the polymer PDLG 5002A, and polymeric nanoparticles loaded with Cabozantinib (CPNs).

4.3.2. CSLNs.

The interpretation of the given FTIR data compares pure Cabozantinib, CSLNs (cabozantinib and lipid nanoparticles), and pure lipid. The wavenumber 3846.33 cm^{-1} for pure

Cabozantinib is often associated with O-H stretching vibrations, possibly indicating the presence of hydroxyl groups, such as those found in alcohols or phenols. The wavenumber 3774.01 cm^{-1} for CSLNs shows a decrease in intensity compared to pure Cabozantinib, suggesting interactions between Cabozantinib and the lipid nanoparticles, affecting O-H stretching clarified in (Figure 7). The same is observed for lipids with a wavenumber of 3433.64 cm^{-1}. The wavenumber 2914.88 cm^{-1} for CSLNs observes a decrease in intensity, indicating changes in aromatic C-H stretching due to interactions with lipid nanoparticles. The values 2853.17 cm^{-1} and 2331.52 cm^{-1} for CSLNs suggest changes in C-H stretching due to interactions with lipid nanoparticles. The wavenumber 1733.69 cm^{-1} for CSLNs observes a change in intensity, indicating interactions between C=O groups in Cabozantinib and the lipid nanoparticles. The value 1464.67 cm^{-1} for CSLNs shows an alteration in intensity, suggesting interactions between C=C groups in Cabozantinib and the lipid nanoparticles. The wavenumber 948.806 cm^{-1} of CSLNs, showing an increase or change in intensity, may suggest interactions or changes in the molecular structure due to the lipid nanoparticles. The wavenumber 829.241 cm^{-1} for the pure drug indicates lower frequency modes associated with rocking vibrations of CH2 groups. It's important to note that the exact functional group assignments can vary depending on the specific chemical structure of Cabozantinib, CSLNs, and lipid nanoparticles.

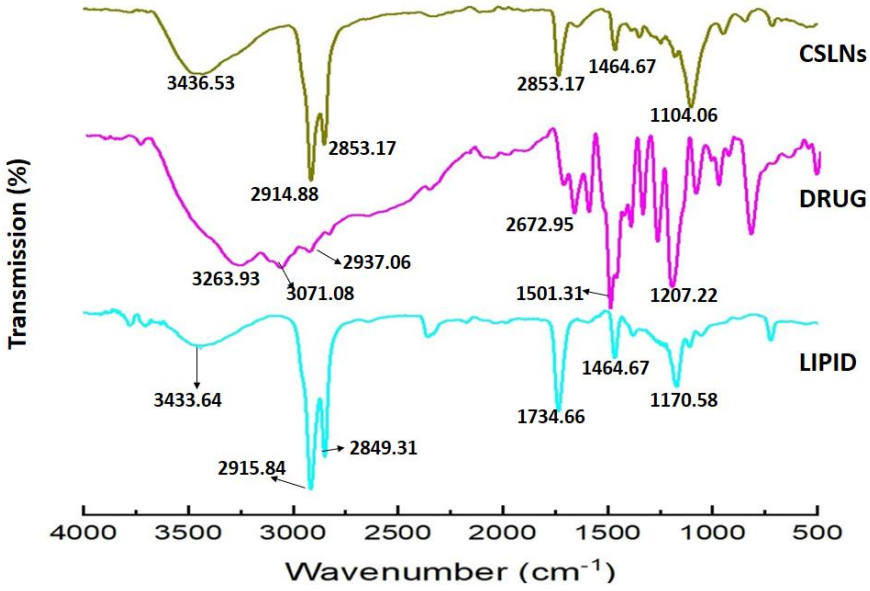

Figure 7. Illustrates the FTIR spectra of Cabozantinib in its original state, the lipid compritol 888, and solid lipid nanoparticles containing loaded Cabozantinib (CSLNs).

4.4. DLS and zeta potential.

As shown in (Figures 8A and 8C), the zeta potentials of the CSLNs and CPNs formulations were found to be -28.7 mV and -9.34 mV, respectively, suggesting a high level of stability. Negative zeta potential nanoparticles usually repress one another, preventing aggregation. Particle sizes in the nanometer range were found to be 64.26 nm for CSLNs and 87.00 nm for CPNs, as shown in (Figures 8B and 8D). PDI values, which are 0.280 for CSLNs and 0.458 for CPNs, indicate that the distribution of particle sizes is comparatively uniform. Furthermore, the quantities of surfactant and co-surfactant probably led to a decrease in surface tension, producing smaller nanoparticles. These findings collectively suggest that CSLNs exhibit better stability and particle size characteristics compared to CPNs tabulated in (Table 5).

Table 5. Provides information on the particle size, PDI, and zeta potential of both CPNs and CSLNs.

Formulation	Particle size (nm)	Polydispersity index	Zeta potential (mv)
CSLNs	64.26	0.280	-28.7
CPNs	87.00	0.458	-9.34

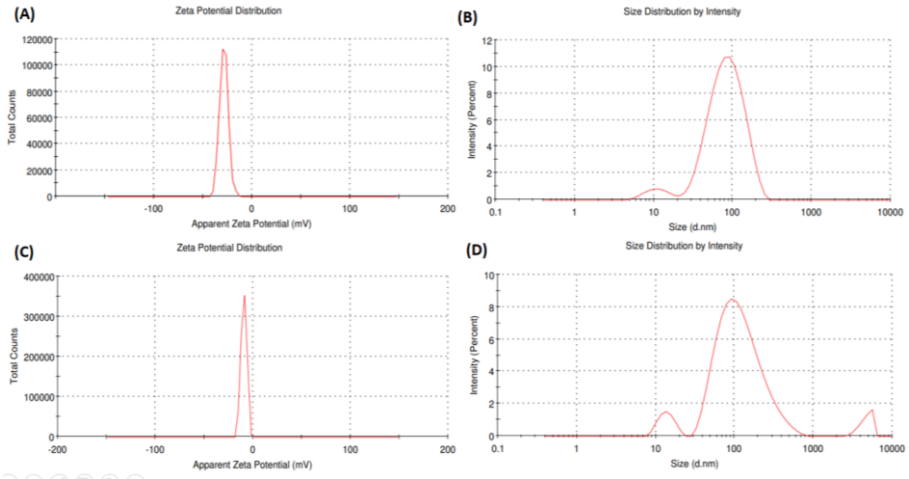

Figure 8. Zeta Potential (ZP), PDI (Polydispersity Index), and Z-average measurements were made of the nanoformulations. The findings are presented as mean values with their standard deviations (SD), as these measurements were performed in triplicate. Part **(A)** shows the CSLNs' Zeta potential, and Part **(B)** shows the CSLNs' DLS. Comparably, while Part **(C)** displays the Zeta potential for CPNs, and Part **(D)** depicts the DLS of CPNs

4.5. TEM.

The internal alignment and surface properties of CSLNs and CPNs were examined using transmission electron microscopy (TEM) research.

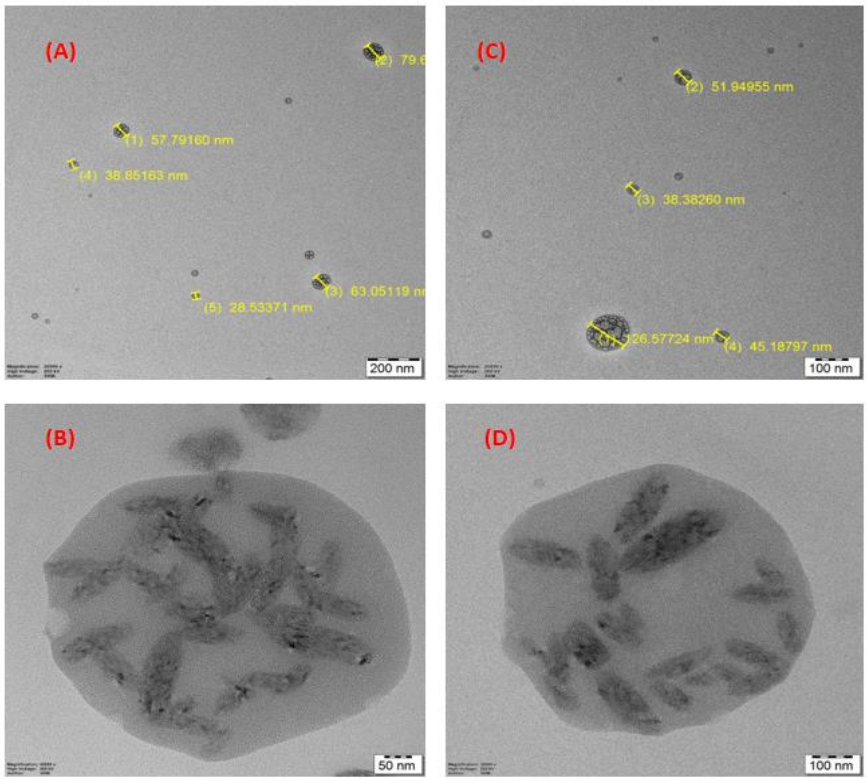

Figure 9. The formulations were subjected to transmission electron microscopy to investigate the following aspects **(A)** Providing a visual representation of the particle size distribution of CSLNs. **(B)** Analyzing the internal structure and surface characteristics of CSLNs. **(C)** offering a visual representation of the particle size distribution of CPNs. **(D)** Examining the internal structure and topographical features of CPNs.

As seen in (Figures 9B and 9D), the pictures show that the nano-formulation particles have smooth surfaces and almost spherical forms, falling within the nanoscale size range. To be more precise, CPNs range from 38 to 126 nm (Figure 9C), whereas CSLNs range from 28 to 79 nm (Figure 9A). Crucially, every particle shows a homogeneous distribution devoid of any structural aberrations. Significantly, CPNs have bigger particle sizes than CSLNs. For the selected drug Cabozantinib, lipid NPs exhibit improved nano-size compared to polymeric nanomaterials.

4.6. Entrapment efficiency (EE) and drug loading (DL).

CSLNs have a pointedly higher EE of 78.11 ± 0.42% with a low standard deviation (p-value = 0.007). This remarkable Competence suggests that lipid nanoparticles can encapsulate a substantial amount of drugs efficiently and steadily. On the other hand, as (Figure 10) shows, CPNs have a slightly higher standard deviation with a p-value of 0.008 and a lower EE of 65.56 ± 2.31%. The structural and chemical differences between lipid and polymer nanoparticles explain the observed differences in EE. Lipid nanoparticles are preferable for drug delivery systems emphasizing stability, consistency, and efficiency as they consistently show lower variability and higher EE. Lipid nanoparticles execute better than polymer nanoparticles in terms of DL, with a DL of 10.15 ± 0.81% and a low p-value of 0.005. Conversely, as tabulated in (Table 6), polymer nanoparticles show a DL of 7.69 ± 0.48%, with a p-value of 0.007, portentous a reduced drug amount per unit of nanoparticles. This recommends that lipid nanoparticles can hold a significant amount of drug per unit of nanoparticles while maintaining a relatively low variable in drug loading.

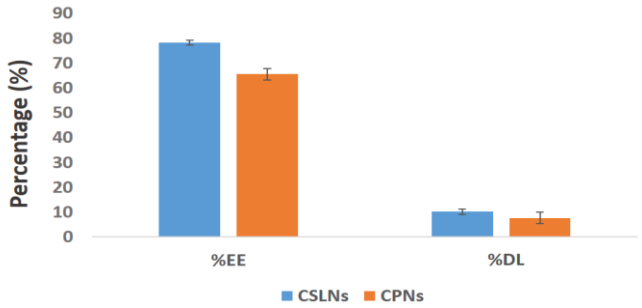

Figure 10. The entrapment efficiency (EE) and drug loading (DL) of both CSLNs and CPNs formulations were evaluated. A statistical analysis using analysis of variance (ANOVA) was accompanied to conclude the implication of the disparities in EE and DL outcomes. These assessments were directed in triplicate (n = 3 independent formulations), and the verdicts are described as mean values with their corresponding standard deviations (SD).

Table 6. Assessment of entrapment efficiency and drug loading capacity for CPNs and CSLNs.

Formulation	Entrapment efficiency	Drug loading
CSLNs	78.11 ± 0.42	10.15 ± 0.81
CPNs	65.56 ± 2.31	7.69 ± 0.48

4.7. In vitro drug release.

At every stage of dissolution, CSLNs demonstrate a substantially higher drug release efficiency than CPNs, with a total release that approaches 99%. Moreover, as (Figure 11) illustrates, CSLNs exhibit high cumulative drug release percentages of 99.52% at 6 hours and 97.99% at 5.5 hours, indicating their remarkable ability to load and transport pharmaceuticals efficiently. Conversely, CPNs exhibit fluctuations in their release kinetics and complete release after four hours and thirty minutes, suggesting a less effective and regulated drug release

mechanism. Particularly for therapeutic applications requiring accurate dosing and regular release, the variability in drug release from CPNs raises doubts about their dependability. A comprehensive scientific analysis of the dissolving data supports the claim that CSLNs perform better than polymer nanoparticles. CSLNs display excellent stability, biocompatibility, regulated, sustained release, and efficiency. Because of these benefits and their exceptional ability to load drugs, lipid nanoparticles are advised for treating HCC.

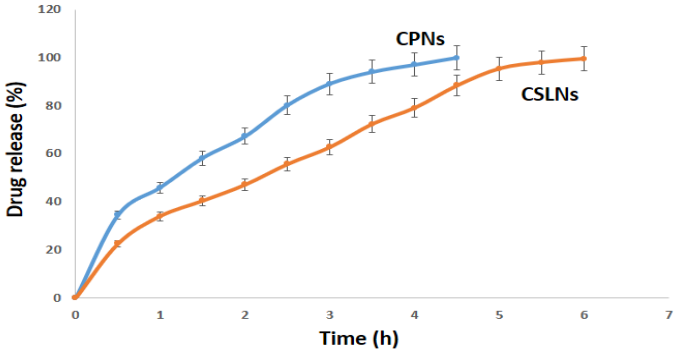

Figure 11. Drug release investigations of CPNs and CSLNs at altered time intervals.

4.8. MTT.

The MTT test findings show that nanoformulations containing cabozantinib have strong anticancer efficacy against the Hep3B cell line. More specifically, as (Figure 12 A) shows, CSLNs had an extremely low IC50 value of 100.55 ± 0.05 µg/mL, demonstrating their strong anticancer activity. This notable outcome is supported by the lipid nanocarriers' efficient transportation of Cabozantinib, which improves penetration into the cell lines. As opposed to CSLNs, CPNs showed a larger IC50 of 140.65 ± 0.05 µg/mL (Figure 12 B), indicating a less potent anticancer activity. Furthermore, as illustrated in (Figure 12 C), pure Cabozantinib had the highest IC50 value of 180.85 ± 0.05 µg/mL, highlighting the benefits of nanoparticle dispersion and the constructive role of nanoformulations in augmenting Cabozantinib anti-HCC efficacy. These results highlight CSLNs' potential as a viable platform for effective and focused cancer treatment.

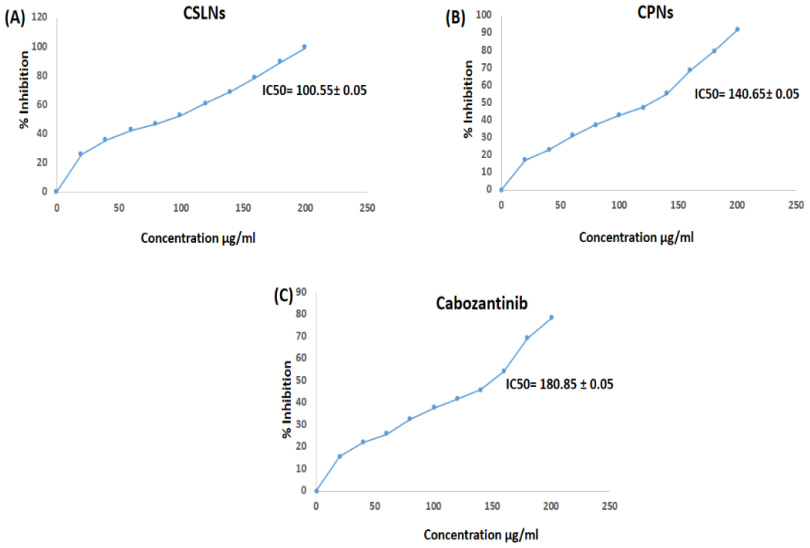

Figure 12. The results of the MTT assay (screen-1) indicate the following outcomes for distinct categories: **(A)** CSLNs, denoting Cabozantinib-loaded solid lipid nanoparticles, demonstrated an IC50 value of 100.55 ± 0.05 µg/mL. **(B)** CPNs, representing Cabozantinib-loaded polymeric nanoparticles, exhibited an IC50 of 140.65 ± 0.05 µg/mL. **(C)** Pure Cabozantinib displayed an IC50 of 180.85 ± 0.05 µg/mL.

4.9. The finding of apoptosis by Annexin V-Cy3 assay.

The cells treated to pure Cabozantinib, CSLNs, and CPNs underwent dual staining with Annexin V-Cy3 and 6-CFDA for 24 hours to identify early apoptotic changes. 6-CFDA staining, on the other hand, serves as a sign of live cells. Annexin V-Cy3 mostly binds to phosphatidylserine that is exposed on the outer membrane surface of treated Hep3B cells during the early stages of apoptosis. Increased Annexin V-Cy3 binding to treated Hep3B cells is suggestive of phosphatidylserine externalization, which is a hallmark of apoptotic cells and is more prevalent in CSLNs than in control and CPNs cells illustrated in (Figure 13). An additional decrease in fluorescence intensity was noted, with CSLNs exhibiting a greater decline than control and CPNs. This decrease is linked to apoptosis using 6-carboxyfluorescein diacetate (6cfda) labeling.

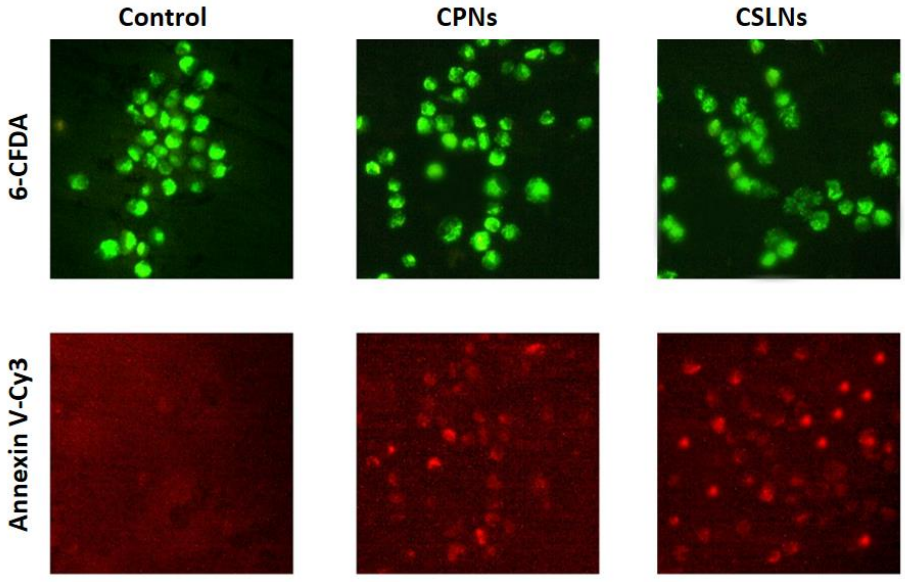

Figure 13. Illustrates fluorescent micrographs depicting the Annexin V-Cy3 apoptosis assay conducted on Hep3B hepatocellular carcinoma (HCC) cell lines after a 24-hour treatment period. Pure Cabozantinib, CPNs, and CSLNs.

5. Conclusions

The high fatality rate of hepatocellular carcinoma (HCC) makes it a serious threat to world health. As a result of the limited effectiveness and adverse effects of conventional chemotherapy, researchers are looking at alternative treatments, such as anticancer drugs based on nanomedicine. Research has demonstrated potential health advantages for liver illnesses, including HCC, with cabotezantinib approved for post-sorafenib treatment in HCC patients. These benefits have been proven using in silico interactions and 100 ns dynamic simulation experiments. In our study, we developed Cabozantinib-loaded polymeric and solid lipid nanoparticles to evaluate their therapeutic effectiveness against HCC.

Comparative analysis revealed that Cabozantinib-loaded solid lipid nanoparticles (CSLNs) outperformed polymeric nanoparticles (PDLG) in terms of encapsulation efficiency (EE) and drug loading (DL) release characteristics. CSLNs exhibited more efficient drug release behavior than Cabozantinib-polymeric nanoparticles (CPNs). *In vitro* cytotoxicity assessments demonstrated that lipid nanoparticles, particularly CSLNs, exhibited enhanced anticancer efficacy with a lower IC50 compared to polymeric nanoparticles, specifically in the Hep3B cell line. The potent anticancer properties of Cabozantinib-loaded lipid nanoparticles

were further validated through fluorescence screening, primarily inducing cell death in Hep3B cells. These findings suggest that solid lipid nanoparticles, especially CSLNs, show promise as nano-formulations targeting HCC. Further research, including relative bioavailability and *in vitro*/in vivo correlation studies, is needed to optimize the effectiveness of polymeric nanoparticles and solid lipid nanoparticles. Nevertheless, our study implies lipid nanoparticles may offer superior anti-malignancy action against HCC.

Funding

The authors received no specific funding for this work.

Acknowledgments

Conceptualization, Writing Methodology, Data curation, and Validation by Mr. Mohammad Habeeb, and Supervision, review, and editing by Dr. Manimaran Vasanthan. The authors are thankful to the Dean and Management of SRM College of Pharmacy, SRM Institute of Science and Technology, Kattankulathur-603203, India, and Crescent School of Pharmacy, B.S. Abdur Rahman Crescent Institute of Science and Technology, Chennai-600048 India.

Conflicts of Interest

The authors declare no conflict of interest

References

1. Chhatwal, J.; Hajjar, A.; Mueller, P.P.; Nemutlu, G.; Kulkarni, N.; Peters, M.L.B.; Kanwal, F. Hepatocellular Carcinoma Incidence Threshold for Surveillance in Virologically Cured Hepatitis C Individuals. *Clinical Gastroenterology and Hepatology* **2023**, doi:10.1016/J.CGH.2023.05.024.
2. Habeeb, M.; Sugumaran, A. Strategies of Cell Signaling and Critical Focus on Etiology of Hepatocellular Carcinoma. **2022**, *12*, 5187–5198, doi:10.33263/BRIAC124.51875198.
3. Radwan, R.R.; Ali, H.E. Radiation-Synthesis of Chitosan/Poly (Acrylic Acid) Nanogel for Improving the Antitumor Potential of Rutin in Hepatocellular Carcinoma. *Drug Deliv Transl Res* **2021**, *11*, 261–278, doi:10.1007/S13346-020-00792-7/METRICS.
4. Almomani, A.; Kumar, P.; Onwuzo, S.; Boustany, A.; Krishtopaytis, E.; Hitawala, A.; Alshaikh, D.; Albakri, A.; Hussein, L.; Hussein, E.; et al. Epidemiology and Prevalence of Lean Nonalcoholic Fatty Liver Disease and Associated Cirrhosis, Hepatocellular Carcinoma, and Cardiovascular Outcomes in the United States: A Population-Based Study and Review of Literature. *Journal of Gastroenterology and Hepatology (Australia)* **2023**, *38*, 269–273, doi:10.1111/JGH.16049.
5. Gromowski, T.; Lukacs-Kornek, V.; Cisowski, J. Current View of Liver Cancer Cell-of-Origin and Proposed Mechanisms Precluding Its Proper Determination. *Cancer Cell Int* **2023**, *23*, doi:10.1186/S12935-022-02843-0.
6. Liu, J.; Qi, W.; Wang, S.; Zhang, Y.; Wang, X.; Sun, D.; Xu, Y.; Shi, J.; Duan, H.; Zhang, Q.; et al. Metabolic Disorders Induced by PNPLA3 and TM6SF2 Gene Variants Affect Chronic Kidney Disease in Patients Infected with Non-Genotype 3 Hepatitis C Virus. *Lipids Health Dis* **2023**, *22*, 91, doi:10.1186/S12944-023-01858-4.
7. Shah, D.D.; Dave, B.P.; Patel, P.A.; Chorawala, M.R.; Patel, V.N.; Shah, P.A.; Patel, M.P. Revamping the Innate or Innate-like Immune Cell-Based Therapy for Hepatocellular Carcinoma: New Mechanistic Insights and Advanced Opportunities. *Medical Oncology* **2023**, *40*, doi:10.1007/S12032-023-01948-4.
8. Pourhamzeh, M.; Asadian, S.; Mirzaei, H.; Minaei, A.; Shahriari, E.; Shpichka, A.; Es, H.A.; Timashev, P.; Hassan, M.; Vosough, M. Novel Antigens for Targeted Radioimmunotherapy in Hepatocellular Carcinoma. *Mol Cell Biochem* **2023**, *478*, 23–37, doi:10.1007/S11010-022-04483-4.
9. Zulaziz, N.; Chai, S.J.; Lim, K.P. The Origins, Roles and Therapies of Cancer Associated Fibroblast in Liver Cancer. *Front Oncol* **2023**, *13*, doi:10.3389/FONC.2023.1151373/FULL.
10. Bailly, C.; Thuru, X. Targeting of Tetraspanin CD81 with Monoclonal Antibodies and Small Molecules to Combat Cancers and Viral Diseases. *Cancers (Basel)* **2023**, *15*, 2186, doi:10.3390/cancers15072186.

11. Kciuk, M.; Gielecińska, A.; Mujwar, S.; Mojzych, M.; Marciniak, B.; Drozda, R.; Kontek, R. Targeting Carbonic Anhydrase IX and XII Isoforms with Small Molecule Inhibitors and Monoclonal Antibodies. *J Enzyme Inhib Med Chem* **2022**, *37*, 1278–1298, doi:10.1080/14756366.2022.2052868.
12. Malvankar, C.; Kumar, D. AXL Kinase Inhibitors- A Prospective Model for Medicinal Chemistry Strategies in Anticancer Drug Discovery. *Biochimica et Biophysica Acta (BBA) - Reviews on Cancer* **2022**, *1877*, 188786, doi:10.1016/j.bbcan.2022.188786.
13. Huang, Y.-C.; Hsieh, P.-Y.; Wang, L.-Y.; Tsai, T.-H.; Chen, Y.-J.; Hsieh, C.-H. Local Liver Irradiation Concurrently Versus Sequentially with Cabozantinib on the Pharmacokinetics and Biodistribution in Rats. *Int J Mol Sci* **2023**, *24*, 5849, doi:10.3390/ijms24065849.
14. Ansari, M.J.; Rahman, M.; Alharbi, K.S.; Altowayan, W.M.; Ali, A.M.A.; Almalki, W.H.; Barkat, M.A.; Singh, T.; Nasar, S.; Akhter, M.H.; et al. Hispolon-Loaded Liquid Crystalline Nanoparticles: Development, Stability, *in vitro* Delivery Profile, and Assessment of Hepatoprotective Activity in Hepatocellular Carcinoma. *ACS Omega* **2022**, *7*, 9452–9464, doi:10.1021/ACSOMEGA.1C06796/ASSET/IMAGES/LARGE/AO1C06796_0008.JPEG.
15. Habeeb, M.; Kareem, T.A.; Deepthi, K.L.; Khot, V.S.; Woon, Y.H.; Pawar, S.S. Nanomedicine for Targeting the Lung Cancer Cells by Interpreting the Signaling Pathways. *J Drug Deliv Sci Technol* **2022**, *77*, 103865, doi:10.1016/J.JDDST.2022.103865.
16. Habeeb, M.; You, H.W.; Aher, K.B.; Bhavar, G.B.; Khot, V.S.; Mishra, S. Strategies of Nanomedicine for Targeting the Signaling Pathways of Colorectal Cancer. *J Drug Deliv Sci Technol* **2023**, *84*, 104487, doi:10.1016/J.JDDST.2023.104487.
17. Wang, B.; Wang, J.; Shao, J.; Kouwer, P.H.J.; Bronkhorst, E.M.; Jansen, J.A.; Walboomers, X.F.; Yang, F. A Tunable and Injectable Local Drug Delivery System for Personalized Periodontal Application. *Journal of Controlled Release* **2020**, *324*, 134–145, doi:10.1016/j.jconrel.2020.05.004.
18. Zaghloul, N.; Mahmoud, A.A.; Elkasabgy, N.A.; El Hoffy, N.M. PLGA-Modified Syloid ® -Based Microparticles for the Ocular Delivery of Terconazole: In-Vitro and in-Vivo Investigations. *Drug Deliv* **2022**, *29*, 2117–2129, doi:10.1080/10717544.2022.2092239.
19. Agrawal, V.; Patel, R.; Patel, M. Design, Characterization, and Evaluation of Efinaconazole Loaded Poly(D, L-Lactide-Co-Glycolide) Nanocapsules for Targeted Treatment of Onychomycosis. *J Drug Deliv Sci Technol* **2023**, *80*, 104157, doi:10.1016/j.jddst.2023.104157.
20. Gebreel, R.M.; Edris, N.A.; Elmofty, H.M.; Tadros, M.I.; El-Nabarawi, M.A.; Hassan, D.H. Development and Characterization of PLGA Nanoparticle-Laden Hydrogels for Sustained Ocular Delivery of Norfloxacin in the Treatment of Pseudomonas Keratitis: An Experimental Study. *Drug Des Devel Ther* **2021**, *Volume 15*, 399–418, doi:10.2147/DDDT.S293127.
21. Fayed, E.A.; Ammar, Y.A.; Saleh, M.A.; Bayoumi, A.H.; Belal, A.; Mehany, A.B.M.; Ragab, A. Design, Synthesis, Antiproliferative Evaluation, and Molecular Docking Study of New Quinoxaline Derivatives as Apoptotic Inducers and EGFR Inhibitors. *JMoSt* **2021**, *1236*, 130317, doi:10.1016/J.MOLSTRUC.2021.130317.
22. Bauer, M.R.; Mackey, M.D. Electrostatic Complementarity as a Fast and Effective Tool to Optimize Binding and Selectivity of Protein-Ligand Complexes. *J Med Chem* **2019**, *62*, 3036–3050, doi:10.1021/ACS.JMEDCHEM.8B01925/SUPPL_FILE/JM8B01925_SI_002.ZIP.
23. Habeeb, M.; Deepthi, K.L.; Vara Prasad, M.V.; Irfan, N.; Liakhat Ali, S.; Navyaja, K. Development Characterization and Molecular Simulation Studies of Metoclopramide HCl and Tramadol HCl Bilayer Tablets. *Res J Pharm Technol* **2022**, 529–534, doi:10.52711/0974-360X.2022.00085.
24. K., S.; B., A.; N.L., S.; Krishna, P.G.; Kareem, A.; Habeeb, M. Investigation of Wrightia Tinctoria Extract Activity on Alopecia Using In-Silco and In-Vivo Studies. *Res J Pharm Technol* **2022**, 643–649, doi:10.52711/0974-360X.2022.00106.
25. Mustafa, G.; Younas, S.; Mahrosh, H.S.; Albeshr, M.F.; Bhat, E.A. Molecular Docking and Simulation-Binding Analysis of Plant Phytochemicals with the Hepatocellular Carcinoma Targets Epidermal Growth Factor Receptor and Caspase-9. *Molecules* **2023**, *28*, 3583, doi:10.3390/molecules28083583.
26. Habeeb, M.; Woon You, H.; Balasaheb Aher, K.; Balasaheb Bhavar, G.; Suryabhan Pawar, S.; Dnyaneshwar Gaikwad, S. Artificial Neural Networks for the Prediction of Mechanical Properties of CGNP/PLGA Nanocomposites. *Mater Today Proc* **2023**, doi:10.1016/j.matpr.2023.08.354.
27. Daoui, O.; Nour, H.; Abchir, O.; Elkhattabi, S.; Bakhouch, M.; Chtita, S. A Computer-Aided Drug Design Approach to Explore Novel Type II Inhibitors of c-Met Receptor Tyrosine Kinase for Cancer Therapy: QSAR, Molecular Docking, ADMET and Molecular Dynamics Simulations. *J Biomol Struct Dyn* **2023**, *41*, 7768–7785, doi:10.1080/07391102.2022.2124456.
28. Mohammad, H.; You, H.W.; Umapathi, M.; Ravikumar, K.K.; Hariyadi; Mishra, S. Strategies of Artificial Intelligence Tools in the Domain of Nanomedicine. *J Drug Deliv Sci Technol* **2023**, 105157, doi:10.1016/j.jddst.2023.105157.
29. Irfan, N.; Balasubramaniyan, S.; Ali, D.M.; Puratchikody, A. Bioisosteric Replacements of Tyrosine Kinases Inhibitors to Make Potent and Safe Chemotherapy against Malignant Cells. *J Biomol Struct Dyn* **2022**, doi:10.1080/07391102.2022.2146751.

30. Nagendran, S.; Balasubramaniyan, S.; Irfan, N. Virtually Screened Novel Sulfathiazole Derivatives as a Potential Drug Candidate for Methicillin-Resistant *Staphylococcus Aureus* and Multidrug-Resistant Tuberculosis. *J Biomol Struct Dyn* **2022**, 1–10, doi:10.1080/07391102.2022.2079002.
31. Okoli, B.J.; Eltayb, W.A.; Gyebi, G.A.; Ghanam, A.R.; Ladan, Z.; Oguegbulu, J.C.; Abdalla, M. In Silico Study and Excito-Repellent Activity of Vitex Negundo L. Essential Oil against Anopheles Gambiae. *Applied Sciences* **2022**, *12*, 7500, doi:10.3390/app12157500.
32. Feczkó, T.; Piiper, A.; Pleli, T.; Schmithals, C.; Denk, D.; Hehlgans, S.; Rödel, F.; Vogl, T.J.; Wacker, M.G. Theranostic Sorafenib-Loaded Polymeric Nanocarriers Manufactured by Enhanced Gadolinium Conjugation Techniques. *Pharmaceutics 2019, Vol. 11, Page 489* **2019**, *11*, 489, doi:10.3390/PHARMACEUTICS11100489.
33. Da Rocha, M.C.O.; Da Silva, P.B.; Radicchi, M.A.; Andrade, B.Y.G.; De Oliveira, J.V.; Venus, T.; Merker, C.; Estrela-Lopis, I.; Longo, J.P.F.; Báo, S.N. Docetaxel-Loaded Solid Lipid Nanoparticles Prevent Tumor Growth and Lung Metastasis of 4T1 Murine Mammary Carcinoma Cells. *J Nanobiotechnology* **2020**, *18*, doi:10.1186/S12951-020-00604-7.
34. Alhelal, H.M.; Mehta, S.; Kadian, V.; Kakkar, V.; Tanwar, H.; Rao, R.; Aldhubiab, B.; Sreeharsha, N.; Shinu, P.; Nair, A.B. Solid Lipid Nanoparticles Embedded Hydrogels as a Promising Carrier for Retarding Irritation of Leflunomide. *Gels* **2023**, *9*, doi:10.3390/GELS9070576.
35. Pandey, P.; Rahman, M.; Bhatt, P.C.; Beg, S.; Paul, B.; Hafeez, A.; Al-Abbasi, F.A.; Nadeem, M.S.; Baothman, O.; Anwar, F.; et al. Implication of Nano-Antioxidant Therapy for Treatment of Hepatocellular Carcinoma Using PLGA Nanoparticles of Rutin. *https://doi.org/10.2217/nnm-2017-0306* **2018**, *13*, 849–870, doi:10.2217/NNM-2017-0306.
36. Bhattacharya, S.; Parihar, V.K.; Prajapati, B.G. Unveiling the Therapeutic Potential of Cabozantinib-Loaded Poly D,L-Lactic-Co-Glycolic Acid and Polysarcosine Nanoparticles in Inducing Apoptosis and Cytotoxicity in Human HepG2 Hepatocellular Carcinoma Cell Lines and in Vivo Anti-Tumor Activity in SCID Female Mice. *Front Oncol* **2023**, *13*, doi:10.3389/fonc.2023.1125857.
37. ML, F. Cabozantinib Loaded DSPE-PEG2000 Micelles as Delivery System: Formulation, Characterization and Cytotoxicity Evaluation. *BAOJ Pharm Sci* **2015**, *1*, 1–9, doi:10.24947/2380-5552/1/1/00101.
38. Gowdhami, B.; Manojkumar, Y.; Vimala, R.T. V.; Ramya, V.; Karthiyayini, B.; Kadalmani, B.; Akbarsha, M.A. Cytotoxic Cobalt (III) Schiff Base Complexes: *In vitro* Anti-Proliferative, Oxidative Stress and Gene Expression Studies in Human Breast and Lung Cancer Cells. *BioMetals* **2022**, *35*, 67–85, doi:10.1007/s10534-021-00351-8.

Supplementary materials

Schrödinger

Simulation Interactions Diagram Report

Simulation Details

Jobname: desmond_md_job_1
Entry title: carbo-5izq

CPU #	Job Type	Ensemble	Temp. [K]	Sim. Time [ns]	# Atoms	# Waters	Charge
1	mdsim	NPT	300.0	100.102	25503	7394	0

Protein Information

Tot. Residues	Prot. Chain(s)	Res. in Chain(s)	# Atoms	# Heavy Atoms	Charge
207	'A'	ict_values([207]	3256	1697	+4

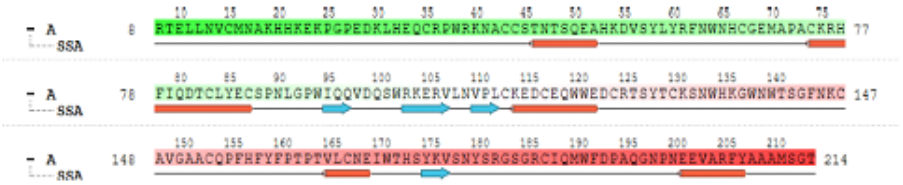

Ligand Information

SMILES	c1cc(F)ccc1NC(=O)C2(CC2)C(=O)Nc3ccc(cc3)Oc4ccnc(c45)cc(OC)c(c5)OC
PDB Name	'UNK'
Num. of Atoms	61 (total) 37 (heavy)
Atomic Mass	501.519 au
Charge	0
Mol. Formula	C28H24FN3O5
Num. of Fragments	5
Num. of Rot. Bonds	10

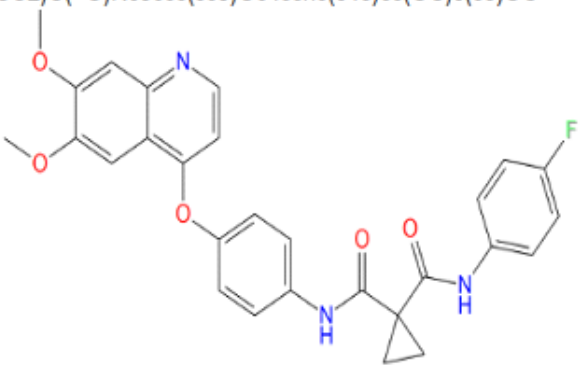

Counter Ion/Salt Information

Type	Num.	Concentration [mM]	Total Charge
Cl	4	9.836	-4

Figure S1. Cabozantinib formed interactions with 19 amino acids of the 5IZQ protein molecule.

Schrödinger

Simulation Interactions Diagram Report

Simulation Details

Jobname: desmond_md_job_1
Entry title: 5abd-carbo

CPU #	Job Type	Ensemble	Temp. [K]	Sim. Time [ns]	# Atoms	# Waters	Charge
1	mdsim	NPT	300.0	100.102	44557	13276	0

Protein Information

Tot. Residues	Prot. Chain(s)	Res. in Chain(s)	# Atoms	# Heavy Atoms	Charge
283	'A', 'B', 'C'	ict_values([95, 93, 95]	4622	2277	+7

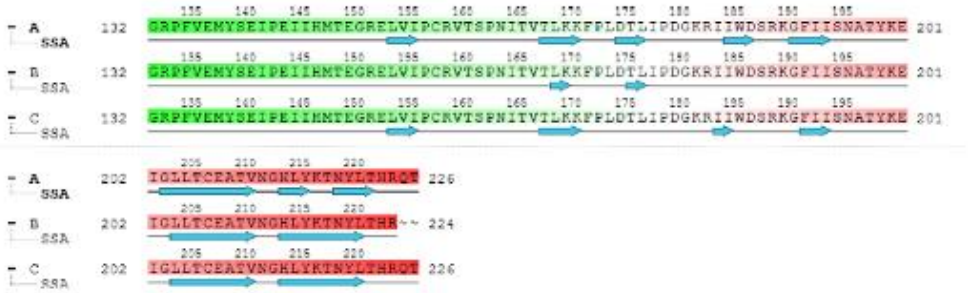

Ligand Information

SMILES	c1cc(F)ccc1NC(=O)C2(CC2)C(=O)Nc3ccc(cc3)Oc4ccnc(c45)cc(OC)c(c5)OC
PDB Name	'UNK'
Num. of Atoms	61 (total) 37 (heavy)
Atomic Mass	501.519 au
Charge	0
Mol. Formula	C28H24FN3O5
Num. of Fragments	5
Num. of Rot. Bonds	10

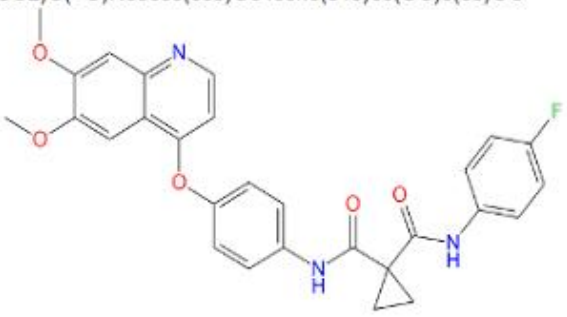

Counter Ion/Salt Information

Type	Num.	Concentration [mM]	Total Charge
O4S	2	2.739	-4
Cl	3	4.109	-3

Figure S2. Cabozantinib formed interactions with 33 amino acids of the 5ABD protein molecule.